SIAM J. SCI. COMPUT.
Vol. 46, No. 2, pp. S1–S23

A ONE-DIMENSIONAL COARSE PRECONDITIONER FOR THREE-DIMENSIONAL UNSTEADY INCOMPRESSIBLE NAVIER–STOKES FLOWS IN PATIENT-SPECIFIC ARTERIES*

YINGZHI LIU†, FENFEN QI†, AND XIAO-CHUAN CAI†‡

Abstract. Numerical simulation of blood flows in patient-specific arteries is becoming an important tool in understanding vascular diseases and surgery planning. Depending on the branching geometry and the patient parameters, the flow can be quite complicated with local vortex structures and rotations, but the principal component of the flow is always along the centerline of the artery. Based on this observation, we introduce a new two-level domain decomposition method for unsteady incompressible Navier–Stokes equations in three-dimensional complex patient-specific arteries, and the key component of the preconditioner is a parameterized one-dimensional unsteady Navier–Stokes or Stokes coarse problem defined along the centerline of the artery. The one-dimensional preconditioner and some overlapping three-dimensional subdomain preconditioners are combined additively to form the two-level method via interpolations using radial basis functions. The most important feature of the method is that the cost of solving the coarse problem is nearly negligible compared with the subdomain solver. The blood flow is modeled by the unsteady incompressible Navier–Stokes equations with resistance outflow boundary conditions discretized by a stabilized finite element method on fully unstructured meshes and the second-order backward differentiation formula in time. Numerical experiments indicate that the proposed method is highly effective and robust for complex arteries with many branches, in other words, the number of linear and nonlinear iterations changes very little when the mesh is refined or the number of subdomains is increased or the number of arterial branches is increased.

Key words. unsteady incompressible Navier–Stokes problem with resistance boundary conditions, blood flows in artery, two-level Schwarz method, parameterized one-dimensional coarse problem, fully implicit finite element method

MSC codes. 76D07, 65N30, 65N55, 65Y05

DOI. 10.1137/22M1496773

1. Introduction.

Early identification can often reduce the probability of the morbidity and mortality of vascular diseases such as peripheral artery disease [43], cerebral aneurysm [25], and coronary artery atherosclerosis [8]. Hemodynamics analysis [1, 15, 44, 55, 60], the study of the behavior of blood flows, can be helpfulin gaining insight into the formation and progression of vascular diseases, and may even identify early as well as make a treatment plan for certain vascular diseases. Many clinical techniques are available for the diagnosis of vascular diseases such as computed tomography, magnetic resonance imaging, transcranial Doppler, and four-dimensional flow magnetic resonance imaging. Recently with the advances in supercomputing and parallel algorithms, tremendous progress has been made on image-based computational fluid dynamics (CFD) methods to study hemodynamics because they are noninvasive and can offer reasonably accurate solutions for clinical applications [41, 45, 46, 47,

*Received by the editors May 18, 2022; accepted for publication (in revised form) October 24, 2022; published electronically July 13, 2023.
https://doi.org/10.1137/22M1496773
Funding: This work was supported in part by FDCT 0141/2020/A3, 0079/2021/AFJ, and NSFC 12201658.

†Department of Mathematics, University of Macau, Macau, People's Republic of China (yingzhiliu@um.edu.mo, yc27956@umac.mo, xccai@um.edu.mo).
‡Corresponding author. Department of Mathematics, University of Macau, Macau, People's Republic of China (xccai@um.edu.mo).

50, 59]. When simulating blood flows using image-based CFD methods, the unsteady incompressible Navier–Stokes equations are often considered with suitable outflow boundary conditions such as the resistance boundary condition and the impedance boundary condition [45, 62]. Taking account of the nonlinearity of the system and the geometrical complexity, the unsteady incompressible Navier–Stokes equations are quite difficult to solve. Many numerical methods have been developed to solve the equations discretized implicitly on fully unstructured meshes. Newton–Krylov methods [35] solve the nonlinear systems by inexact Newton methods in which the Jacobian systems are solved by a Krylov subspace method with suitable preconditioner, for example, block preconditioners [10, 11, 14, 32, 33], multigrid preconditioners [36], and overlapping Schwarz preconditioners (NKS) [3, 5]. Projection methods [26, 48, 49] split the discretized problem into some smaller problems involving the velocity and pressure fields and then approximately solve them successively. We also mention that there are many other methods for the hemodynamics simulation including lattice Boltzmann methods [51], dual-primal FETI methods [2], BDDC methods [40], multigrid methods [21], and isogeometric methods [63]. Taking advantage of Newton methods [9], Krylov subspace methods [54], and domain decomposition methods [61], in this paper, we solve the unsteady incompressible Navier–Stokes equations in patient-specific arteries by NKS and focus on the construction of a two-level additive Schwarz preconditioner with a highly effective, robust, and low cost coarse preconditioner.

In two-level additive Schwarz preconditioners, the coarse problem together with its restriction and extension plays a crucial role in the overall performance. In [27, 28], a monolithic overlapping Schwarz preconditioner with generalized Dryja–Smith–Widlund (GDSW) coarse spaces was introduced and studied, the method was inspired by the original GDSW coarse spaces [12], and the monolithic Schwarz preconditioner [34, 37, 38] introduced a coarse problem by discretizing the original problem in a geometry-preserving three-dimensional coarse mesh. Since the geometries of the coarse and fine meshes match each other, the restriction and extension matrices can be constructed by the finite element basis functions of the coarse mesh. [7] presented a nonnested coarse mesh to reduce the number of mesh points of the geometry-preserving coarse mesh near the wall and the restriction and extension matrices are defined using radial basis functions to deal with the nonmatching geometries of the coarse and fine meshes. All the coarse meshes developed in [7, 37, 38] are three dimensional and solving these coarse problems takes a significant percentage of the overall compute time.

Recently, for steady Stokes equations in two-dimensional tube-like domains, we introduced a coarse problem based on the parameterized one-dimensional steady Stokes equations defined on the centerline of the domain, and showed that the method is quite effective in reducing the number of iterations and the cost of the coarse preconditioner is nearly negligible [42]. In fact, as cheap approximations of complex blood flows in three-dimensional arteries, one-dimensional models have been studied widely [17, 18, 56, 58]. However, limited by the characteristics of one-dimensional models, most of the studies focus on the global behaviors of the flow such as the averaged pressure and the flow waveforms [52, 53] or combining the one-dimensional model with three-dimensional models to simulate blood flows in multiscale arteries [16]. In this paper, we extend the idea of the one-dimensional coarse preconditioner to a one-dimensional unsteady Navier–Stokes model to solve the unsteady incompressible Navier–Stokes equations in three-dimensional patient-specific arteries. The full three-dimensional Navier–Stokes model is sometimes necessary especially for exploring the localized

hemodynamic quantities such as the wall shear stress, local vortex dynamics, and flow rotations in patient-specific arteries [24, 55].

The one-dimensional model of the unsteady incompressible Navier–Stokes equations on the centerline of an artery with multiple branches is obtained by a homogenization of the three-dimensional unsteady incompressible Navier–Stokes model on the cross section with suitable compatibility conditions at bifurcations. We then use a fully discretized matrix of the one-dimensional model to construct the one-dimensional coarse preconditioner with appropriate restrictions and extension matrices between the one-dimensional coarse mesh and the three-dimensional fine mesh. Experiments show that the method works quite well even for situations with a large number of branches. It is known that in a cardiac cycle, the flow is usually easier to model in the diastole phase than the systole phase, and the proposed method works well in both phases. This type of robustness is important for clinical applications.

The rest of the paper is organized as follows. In section 2 we describe the model problem and the stabilized finite element discretization. In section 3 we briefly recall the Newton–Krylov–Schwarz method and focus on the details of the one-dimensional coarse preconditioner. Section 4 shows some numerical experiments for patient-specific arteries to verify the effectiveness and robustness of the one-dimensional coarse preconditioner. Some concluding remarks are given in section 5.

2. Unsteady incompressible Navier–Stokes model with resistance outflow boundary condition and its stabilized finite element discretization. Consider the unsteady imcompressible Navier–Stokes problem in an arterial domain $\Omega \in \mathbb{R}^3$ (see Figure 1),

$$\begin{cases} \rho\left(\dfrac{\partial \boldsymbol{u}}{\partial t} + \boldsymbol{u}\cdot\nabla\boldsymbol{u}\right) - \nu\Delta\boldsymbol{u} + \nabla p = \boldsymbol{f} & \text{in } \Omega\times(0,T), \\ \nabla\cdot\boldsymbol{u} = \boldsymbol{0} & \text{in } \Omega\times(0,T), \\ \boldsymbol{u}(\boldsymbol{x},0) = \boldsymbol{u}_0(\boldsymbol{x}) & \text{in } \Omega, \end{cases} \tag{2.1}$$

where $\boldsymbol{u}$ and p are the velocity and pressure, $\boldsymbol{f}$ and $\boldsymbol{u}_0$ are the given source term and initial velocity, ρ and ν are the blood density and viscosity coefficient. Denote by $\partial\Omega = \Gamma_I \cup \Gamma_W \cup \Gamma_O$ the boundary of the domain, where Γ_I, Γ_W, and $\Gamma_O = \bigcup_{i=1}^{m} \Gamma_O^i$ are the inlet boundary, the arterial wall, and the m outlet boundaries, respectively. On the boundaries, we impose a Dirichlet condition for the inlet velocity, a no-slip condition on the wall velocity, and a resistance condition on the outlet pressure; more precisely, we have the following conditions:

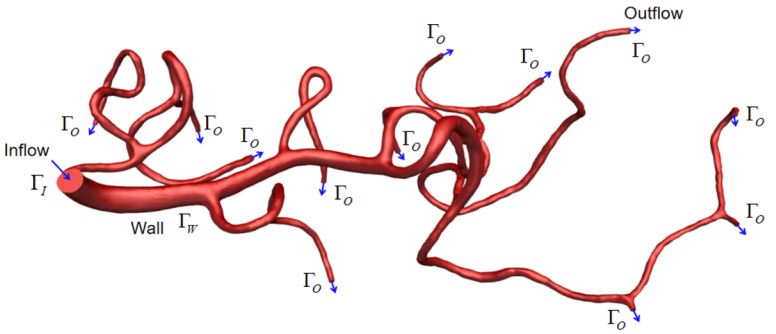

FIG. 1. *A sample artery with* 1 *inlet and* 12 *outlets.*

$$\boldsymbol{u} = \boldsymbol{u}_I \quad \text{on } \Gamma_I \times (0,T), \tag{2.2}$$

$$\boldsymbol{u} = 0 \quad \text{on } \Gamma_W \times (0,T), \tag{2.3}$$

$$p = R_i Q_i \quad \text{on } \Gamma_O^i \times (0,T), \tag{2.4}$$

where $\boldsymbol{u}_I$ is the inlet velocity, R_i is the constant resistance, and $Q_i = \int_{\Gamma_O^i} \boldsymbol{u} \cdot \boldsymbol{n} \mathrm{d}\Gamma_O^i$ is the fluid flux at the local outlet surface Γ_O^i with the outward unit normal vector $\boldsymbol{n}$.

Before introducing the weak form of (2.1), we define $\boldsymbol{H}_W^1(\Omega) = \{\boldsymbol{v} \in \boldsymbol{H}^1(\Omega) : \boldsymbol{v}|_{\Gamma_I} = \boldsymbol{u}_I, \boldsymbol{v}|_{\Gamma_W} = 0\}$, $\boldsymbol{H}_{IW}^1(\Omega) = \{\boldsymbol{v} \in \boldsymbol{H}^1(\Omega) : \boldsymbol{v}|_{\Gamma_I \cup \Gamma_W} = 0\}$. Then the variational formulation of (2.1) with boundary conditions (2.2)–(2.4) is to find $(\boldsymbol{u}(\cdot,t), p(\cdot,t)) \in \boldsymbol{H}_W^1(\Omega) \times L^2(\Omega)$ such that

$$\begin{aligned} &\left(\rho \frac{\partial \boldsymbol{u}}{\partial t}, \boldsymbol{v}\right) + (\nu \nabla \boldsymbol{u}, \nabla \boldsymbol{v}) - (p, \nabla \cdot \boldsymbol{v}) + (q, \nabla \cdot \boldsymbol{u}) + (\rho \boldsymbol{u} \cdot \nabla \boldsymbol{u}, \boldsymbol{v}) \\ &- \langle \nu \nabla \boldsymbol{u} \cdot \boldsymbol{n}, \boldsymbol{v} \rangle_{\Gamma_O} + \sum_{i=1}^{m} R_i \int_{\Gamma_O^i} \boldsymbol{u} \cdot \boldsymbol{n} \mathrm{d}\Gamma_O^i \int_{\Gamma_O^i} \boldsymbol{v} \cdot \boldsymbol{n} \mathrm{d}\Gamma_O^i = (\boldsymbol{f}, \boldsymbol{v}) \end{aligned} \tag{2.5}$$

for all $(\boldsymbol{v}, q) \in \boldsymbol{H}_{IW}^1(\Omega) \times L^2(\Omega)$ and $t \in (0,T)$, where $(u,v) := \int_\Omega uv \mathrm{d}\Omega$ and $\langle u, v \rangle_\Gamma := \int_\Gamma uv \mathrm{d}\Gamma$.

Let $\mathcal{T}_h$ be a shape-regular unstructured tetrahedral mesh of Ω, and the continuous, piecewise linear polynomial function space on $\mathcal{T}_h$ is denoted by S_h. We define the finite element spaces $\boldsymbol{V}_h = [S_h]^3 \cap \boldsymbol{H}_W^1(\Omega)$, $\boldsymbol{W}_h = [S_h]^3 \cap \boldsymbol{H}_{IW}^1(\Omega)$ for the velocity and $Q_h = S_h \cap L^2(\Omega)$ for the pressure. Considering the advantages of the low- and equal-order finite element pair in terms of the computational complexity and the ease of implementation compared with the stable finite element pairs, following [7, 19], we use the stabilized finite element method to spatially discretize the weak formulation (2.5), that is, to find $(\boldsymbol{u}_h(\cdot,t), p_h(\cdot,t)) \in \boldsymbol{V}_h \times Q_h$, such that

$$\begin{cases} \left(\rho \dfrac{\partial \boldsymbol{u}_h}{\partial t}, \boldsymbol{v}_h\right) + (\nu \nabla \boldsymbol{u}_h, \nabla \boldsymbol{v}_h) - (p_h, \nabla \cdot \boldsymbol{v}_h) + (q_h, \nabla \cdot \boldsymbol{u}_h) + (\rho \boldsymbol{u}_h \cdot \nabla \boldsymbol{u}_h, \boldsymbol{v}_h) \\ -\langle \nu \nabla \boldsymbol{u}_h \cdot \boldsymbol{n}, \boldsymbol{v}_h \rangle_{\Gamma_O} + \displaystyle\sum_{i=1}^{m} R_i \int_{\Gamma_O^i} \boldsymbol{u}_h \cdot \boldsymbol{n} \mathrm{d}\Gamma_O^i \int_{\Gamma_O^i} \boldsymbol{v}_h \cdot \boldsymbol{n} \mathrm{d}\Gamma_O^i \\ + \displaystyle\sum_{K \in \mathcal{T}_h} \left(\rho \left(\frac{\partial \boldsymbol{u}_h}{\partial t} + \boldsymbol{u}_h \cdot \nabla \boldsymbol{u}_h\right) + \nabla p_h, \gamma_1 (\boldsymbol{u}_h \cdot \nabla \boldsymbol{v}_h + \nabla q_h)\right)_K \\ + \displaystyle\sum_{K \in \mathcal{T}_h} (\nabla \cdot \boldsymbol{u}_h, \gamma_2 \nabla \cdot \boldsymbol{v}_h)_K \\ = (\boldsymbol{f}, \boldsymbol{v}_h) + \displaystyle\sum_{K \in \mathcal{T}_h} (\boldsymbol{f}, \gamma_1 (\boldsymbol{u}_h \cdot \nabla \boldsymbol{v}_h + \nabla q_h))_K \end{cases} \tag{2.6}$$

for all $(\boldsymbol{v}_h, q_h) \in \boldsymbol{W}_h \times Q_h$ and $t \in (0,T)$. Here the stabilization parameters γ_1 and γ_2 are defined as

$$\gamma_1 = \left(\sqrt{\frac{4}{\triangle t^2} + \boldsymbol{u}_h^T \mathbf{G} \boldsymbol{u}_h + 36 \left(\frac{\nu}{\rho}\right)^2 \mathbf{G} : \mathbf{G}}\right)^{-1}, \gamma_2 = \left(8 \gamma_1 \sum_{i=1}^{3} \mathrm{G}_{i,i}\right)^{-1},$$

where $\mathbf{G} = (\mathrm{G}_{i,j}), (i,j = 1,2,3)$ is the covariant metric tensor satisfying $\mathrm{G}_{i,j} = \sum_{k=1}^{3} \frac{\partial \hat{x}_k}{\partial x_i} \frac{\partial \hat{x}_k}{\partial x_j}$, $\{\hat{x}_i\}_{i=1}^3$ and $\{x_i\}_{i=1}^3$ are the local reference and global physical coordinate variables, respectively. Let $\{\varphi_i\}_{i=1}^N$ be the basis functions, where N is the number of mesh points. Then the numerical solution $\boldsymbol{u}_h$ and p_h can be written

as $\boldsymbol{u}_h(t,x) = \sum_{i=1}^{N}(U_i(t), V_i(t), W_i(t))\varphi_i(x)$ and $p_h(t,x) = \sum_{i=1}^{N} P_i(t)\varphi_i(x)$, where $U = (U_i), V = (V_i), W = (W_i)$, and $P = (P_i)$ are the vectors of the nodal values of the velocity unknowns and the pressure unknowns, respectively. Define $X = (U, V, W, P)^T$ and then (2.6) can be rewritten as a system of ordinary differential equations

$$\frac{dX}{dt} = L(X). \tag{2.7}$$

Considering the numerical accuracy, instead of the implicit backward Euler formula, we use the second-order backward differentiation formula (BDF2) for the temporal discretization with the time step size $\triangle t$, then the fully discretized system at $t = n\triangle t$ is given by

$$\frac{\frac{3}{2}X^n - 2X^{n-1} + \frac{1}{2}X^{n-2}}{\triangle t} = L(X^n) \quad (n \geq 2), \tag{2.8}$$

where X^1 can be obtained by the first-order implicit Euler method with the given initial value X^0.

3. Implicit solver with a two-level Schwarz preconditioner. The nonlinear algebraic system (2.8) is large, sparse, and quite difficult to solve because its underlying arterial geometry is complex and its solution involves highly nonlinear features. In a cardiac cycle, many systems of form (2.8) need to be constructed and solved, and some of them are relatively easy to solve but others are difficult to solve, therefore a robust nonlinear solver is important for the simulation of the blood flow in a whole cardiac cycle. Rewrite the nonlinear system (2.8) as

$$F^n(X^n) = 0. \tag{3.1}$$

The general framework of the nonlinear solver [5] can be described as follows.

In Algorithm 3.1, J_k^n is the analytically constructed Jacobian matrix of the nonlinear system F^n at X_k^n, $(M_k^n)^{-1}$ is a preconditioner to be discussed later, f is a merit function defined as $f(X) = \|F(X)\|_2^2/2$, and ε is a control parameter with a default value $\varepsilon = 10^{-4}$. The user-defined absolute and relative tolerances $atol_{\text{GMRES}}, rtol_{\text{GMRES}}$ and $atol_{\text{Newton}}, rtol_{\text{Newton}}$ are used to control the Krylov and Newton iterations, respectively.

In order to construct an efficient preconditioner M_k^n at each Newton step, we consider a two-level overlapping additive Schwarz preconditioner of the form $M^{-1} = M_{cl}^{-1} + M_{1s}^{-1}$, where M_{cl}^{-1} is a one-dimensional coarse preconditioner and M_s^{-1} is the sum of some three-dimensional subdomain preconditioners, which will be introduced in the following subsections.

3.1. One-dimensional coarse preconditioner. We consider a coarse preconditioner of the form

$$M_{cl}^{-1} = E_{cl} A_{cl}^{-1} R_{cl}, \tag{3.5}$$

where A_{cl} is the discretized matrix of a coarse problem, R_{cl} and E_{cl} are the restriction and extension matrices between the coarse and fine finite element spaces, respectively. In this subsection, we focus on the construction of a coarse preconditioner in which A_{cl} is derived from discretizing a parameterized one-dimensional unsteady Navier–Stokes coarse problem defined on the centerline of the artery. The problem is obtained by

Algorithm 3.1 Inexact Newton for $F^n(X^n)=0$

1: Give an initial guess $X_0^n = X^{n-1}$.
2: **for** $k=0,1,2,\ldots$ **do**
3: Find the Newton direction s_k^n by solving the Jacobian system by a preconditioned restarted GMRES method

$$J_k^n \left(M_k^n\right)^{-1} M_k^n s_k^n = -F^n(X_k^n) \tag{3.2}$$

with the stopping criterion

$$\|F^n(X_k^n) + J_k^n s_k^n\|_2 \le \max\left\{atol_{\text{GMRES}}, rtol_{\text{GMRES}} \|F^n(X_k^n)\|_2\right\}. \tag{3.3}$$

4: Find the step size λ_k^n by the line search technique (Armijo rule)

$$f(X_k^n + \lambda_k^n s_k^n) \le f(X_k^n) + \varepsilon \lambda_k^n \nabla f(X_k^n)^T s_k^n. \tag{3.4}$$

5: Update the Newton solution $X_{k+1}^n = X_k^n + \lambda_k^n s_k^n$.
6: **if** $\|F^n(X_{k+1}^n)\|_2 < \max\{atol_{\text{Newton}}, rtol_{\text{Newton}} \|F^n(X_0^n)\|_2\}$ **then**
7: $X^n = X_{k+1}^n$, return.
8: **end if**
9: **end for**

an approximate integration of the three-dimensional Navier–Stokes equations on the cross section centered at a point on the centerline.

3.1.1. One-dimensional parameterized unsteady incompressible Navier–Stokes equations and their discretization. Denote Ω_{cl} as the centerline of Ω, which is a curve in the three-dimensional (3D) space parameterized by the arc length s, $C_s(s)$ as the cross section of Ω, and $A_s(s)$ as the corresponding area. Let $u^{cl}(t,s)$ be the tangential component of the velocity along the centerline and $p^{cl}(t,s)$ be the value of the pressure on the centerline. We assume that the pressure is a constant on each cross section and the velocity consists mainly of the component u_s along the centerline, i.e., $\boldsymbol{u} \approx u_s \boldsymbol{\tau}$, where $\boldsymbol{\tau} = (\tau^1, \tau^2, \tau^3)$ is the unit tangent vector along the centerline. Further we assume that the component u_s has a parabolic profile at each cross section, i.e.,

$$u_s(t,r,s) = u^{cl}(t,s)\zeta\left(\frac{r}{r_0(s)}\right), \tag{3.6}$$

where $\zeta(y) = (1-y^2)$ $(y \in [0,1])$ is a parabolic profile function, $r_0(s)$ is the radius of $C_s(s)$, and r is the radial coordinate with respect to $C_s(s)$. Define $Q = \int_{C_s} u_s \mathrm{d}C_s$ as the flux on the cross section C_s. For a nonbifurcating artery Ω (see the left subfigure in Figure 2), the one-dimensional unsteady Navier–Stokes model on the centerline Ω_{cl} can be described as [42, 46]

$$\begin{cases} \rho \dfrac{\partial Q}{\partial t} + \beta\rho\alpha \dfrac{\partial}{\partial s}\left(\dfrac{Q^2}{A_s}\right) + K_r \dfrac{Q}{A_s} + A_s \dfrac{\partial p^{cl}}{\partial s} = f^{cl}, \\ \dfrac{\partial Q}{\partial s} = 0,\ u^{cl}(s,0) = u_0^{cl}(s), \end{cases} \tag{3.7}$$

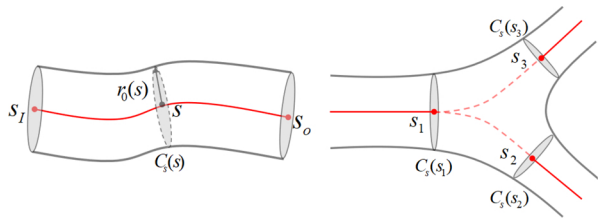

FIG. 2. *A nonbifurcating (left) and a bifurcating (right) artery with the marked centerline and cross sections.*

where $\alpha = 4/3$ is the Coriolis coefficient, $K_r = 8\pi\nu$, $f^{cl} = \int_{C_s} \boldsymbol{f} \cdot \boldsymbol{\tau} \mathrm{d}C_s$ and $u_0^{cl} = \int_{C_s} \boldsymbol{u}_0 \cdot \boldsymbol{\tau} \mathrm{d}C_s$. Here $\beta = 0$ represents the one-dimensional Stokes model and $\beta = 1$ represents the Navier–-Stokes model. By the flux conservation equation $\frac{\partial Q}{\partial s} = 0$, the nonlinear term $\frac{\partial}{\partial s}(\frac{Q^2}{A_s})$ in (3.7) can be reduced to $Q\frac{\partial}{\partial s}(\frac{Q}{A_s})$. Based on the assumption (3.6), we have $Q = A_s u^{cl}/2$, and (3.7) can be rewritten as

$$\begin{cases} \rho\dfrac{A_s}{2}\dfrac{\partial u^{cl}}{\partial t} + \beta\rho\dfrac{\alpha}{4}A_s u^{cl}\dfrac{\partial u^{cl}}{\partial s} + \dfrac{K_r}{2}u^{cl} + A_s\dfrac{\partial p^{cl}}{\partial s} = f^{cl}, \\ \dfrac{\partial(A_s u^{cl})}{\partial s} = 0, \ u^{cl}(s,0) = u_0^{cl}(s). \end{cases} \tag{3.8}$$

At the inlet point s_I and the outlet point s_o of the centerline, we consider the following boundary conditions,

$$u^{cl}(s_I,t) = -\frac{2}{|\Gamma_I|}\int_{\Gamma_I} \boldsymbol{u}_I \cdot \boldsymbol{n} \mathrm{d}\Gamma_I := u_I^{cl}, \tag{3.9}$$

$$p^{cl}(s_o,t) = R_o Q_o \approx \frac{R_o A_s(s_o)}{2} u^{cl}(s_o,t), \tag{3.10}$$

obtained by integrating (2.2) on the inlet boundary and (2.4) on the outlet boundary.

Define the centerline velocity function spaces $\mathrm{M}(\Omega_{cl}) = \{v^{cl} \in H^1(\Omega_{cl})\colon v^{cl}(s_I) = u_I^{cl}\}$, $\mathrm{M}_0(\Omega_{cl}) = \{v^{cl} \in H^1(\Omega_{cl}) : v^{cl}(s_I) = 0, v^{cl}(s_o) = 0\}$. Then the variational formulation of the one-dimensional problem (3.8) with the boundary conditions (3.9)–(3.10) is to find $(u^{cl}(\cdot,t), p^{cl}(\cdot,t)) \in \mathrm{M}(\Omega_{cl}) \times L^2(\Omega_{cl})$ such that

$$\begin{cases} \left(\rho\dfrac{A_s}{2}\dfrac{\partial u^{cl}}{\partial t}, v^{cl}\right) + \beta\left(\rho\dfrac{\alpha}{4}A_s u^{cl}\dfrac{\partial u^{cl}}{\partial s}, v^{cl}\right) + \left(\dfrac{K_r}{2}u^{cl}, v^{cl}\right) \\ \quad + A_s v^{cl} p^{cl}\Big|_{s_I}^{s_o} - \left(\dfrac{\partial(A_s v^{cl})}{\partial s}, p^{cl}\right) + \left(\dfrac{\partial(A_s u^{cl})}{\partial s}, q^{cl}\right) = \left(f^{cl}, v^{cl}\right), \\ \dfrac{R_o A_s(s_o)}{2}u^{cl}(s_o) - p^{cl}(s_o) = 0 \end{cases} \tag{3.11}$$

for all $(v^{cl}, q^{cl}) \in \mathrm{M}_0(\Omega_{cl}) \times L^2(\Omega_{cl})$ and $t \in (0,T)$. Let $\mathcal{T}_h^{cl}$ be a polyline mesh for Ω_{cl} with the mesh size $O(h_{cl})$ and S_h^{cl} be the corresponding continuous, piecewise linear polynomial function space. Define the finite element spaces $V_h^{cl} = S_h^{cl} \cap \mathrm{M}(\Omega_{cl}), W_h^{cl} = S_h^{cl} \cap \mathrm{M}_0(\Omega_{cl})$ for the velocity and $Q_h^{cl} = S_h^{cl} \cap L^2(\Omega_{cl})$ for the pressure. The stabilized finite element discretization of the weak formulation (3.11) is written as find $(u_h^{cl}(\cdot,t), p_h^{cl}(\cdot,t)) \in V_h^{cl} \times Q_h^{cl}$, such that

$$
\begin{cases}
\left(\rho\dfrac{A_s}{2}\dfrac{\partial u_h^{cl}}{\partial t}, v_h^{cl}\right) + \beta\left(\rho\dfrac{\alpha}{4}A_s u_h^{cl}\dfrac{\partial u_h^{cl}}{\partial s}, v_h^{cl}\right) + \left(\dfrac{K_r}{2}u_h^{cl}, v_h^{cl}\right) \\
+\left(A_s v_h^{cl}, \dfrac{\partial p_h^{cl}}{\partial s}\right) - \left(A_s u_h^{cl}, \dfrac{\partial q_h^{cl}}{\partial s}\right) + A_s u_h^{cl} q_h^{cl}\Big|_{s_I}^{s_o} \\
+\gamma_{cl}\displaystyle\sum_{e\in\mathcal{T}_h^{cl}}\left(\rho\dfrac{A_s}{2}\dfrac{\partial u_h^{cl}}{\partial t} + \beta\rho\dfrac{\alpha}{4}A_s u_h^{cl}\dfrac{\partial u_h^{cl}}{\partial s} + \dfrac{K_r}{2}u_h^{cl} + A_s\dfrac{\partial p_h^{cl}}{\partial s}, h_{cl}^2\dfrac{\partial q_h^{cl}}{\partial s}\right)_e \\
= \left(f^{cl}, v_h^{cl}\right) + \gamma_{cl}\displaystyle\sum_{e\in\mathcal{T}_h^{cl}}\left(f^{cl}, h_{cl}^2\dfrac{\partial q_h^{cl}}{\partial s}\right)_e, \\
\dfrac{R_o A_s(s_o)}{2}u_h^{cl}(s_o) - p_h^{cl}(s_o) = 0
\end{cases} \tag{3.12}
$$

for all $(v_h^{cl}, q_h^{cl}) \in W_h^{cl} \times Q_h^{cl}$ and $t \in (0,T)$, where $\gamma_{cl} > 0$ is a stabilization parameter. Using the implicit first-order backward Euler method for the temporal discretization with the time step size $\triangle t$, we have a linearized and fully discretized scheme of (3.12) at $t = n\triangle t$,

$$
\begin{cases}
\mathcal{B}_{cl}\left(u_h^{cl,n}, p_h^{cl,n}; v_h^{cl}, q_h^{cl}\right) = \left(F_{cl}, v_h^{cl}\right) + \gamma_{cl}\displaystyle\sum_{e\in\mathcal{T}_h^{cl}}\left(F_{cl}, h_{cl}^2\dfrac{\partial q_h^{cl}}{\partial s}\right)_e, \\
\dfrac{R_o A_s(s_o)}{2}u_h^{cl,n}(s_o) - p_h^{cl,n}(s_o) = 0,
\end{cases} \tag{3.13}
$$

where

$$
F_{cl} = f^{cl} + \rho\frac{A_s}{2\triangle t}u_h^{cl,n-1} + \beta\rho\frac{\alpha}{4}A_s u_h^{cl,n-1}\frac{\partial}{\partial s}\left(u_h^{cl,n-1}\right)
$$

and

$$
\begin{aligned}
\mathcal{B}_{cl}\left(u_h^{cl,n}, p_h^{cl,n}; v_h^{cl}, q_h^{cl}\right) = \left(B_{cl}, v_h^{cl}\right) + \gamma_{cl}\sum_{e\in\mathcal{T}_h^{cl}}\left(B_{cl}, h_{cl}^2\frac{\partial q_h^{cl}}{\partial s}\right)_e - \left(A_s u_h^{cl,n}, \frac{\partial q_h^{cl}}{\partial s}\right) \\
+ A_s u_h^{cl,n} q_h^{cl}\Big|_{s_I}^{s_o}
\end{aligned}
$$

with

$$
B_{cl} = \rho\frac{A_s}{2\triangle t}u_h^{cl,n} + \beta\rho\frac{\alpha}{4}A_s\left(u_h^{cl,n-1}\frac{\partial}{\partial s}\left(u_h^{cl,n}\right) + u_h^{cl,n}\frac{\partial}{\partial s}\left(u_h^{cl,n-1}\right)\right) + \frac{K_r}{2}u_h^{cl,n} + A_s\frac{\partial p_h^{cl,n}}{\partial s}.
$$

The coarse matrix A_{cl} is simply the matrix form of (3.13). The linearized term (i.e., the second term in B_{cl}) corresponds to the nonlinear term in (3.8). When $\beta = 0$, this term vanishes and the matrix A_{cl} degenerates into the one-dimensional Stokes matrix.

For general bifurcating arterial networks, the one-dimensional model can be derived by combining the one-dimensional (1D) model (3.8) at each nonbifurcating branch with suitable compatibility conditions on each bifurcation. To briefly describe the conditions, we assume that there is one inflow branch and two outflow branches on each bifurcation (see the right subfigure in Figure 2), then using the conservation of flux and the continuity of the pressure [17, 42] on each bifurcation, we have the compatibility conditions

$$
A_s(s_1)u^{cl}(s_1) = A_s(s_2)u^{cl}(s_2) + A_s(s_3)u^{cl}(s_3), \quad p^{cl}(s_1) = p^{cl}(s_2) = p^{cl}(s_3). \tag{3.14}
$$

For more general bifurcations involving more bifurcating branches, similar compatibility conditions can also be given.

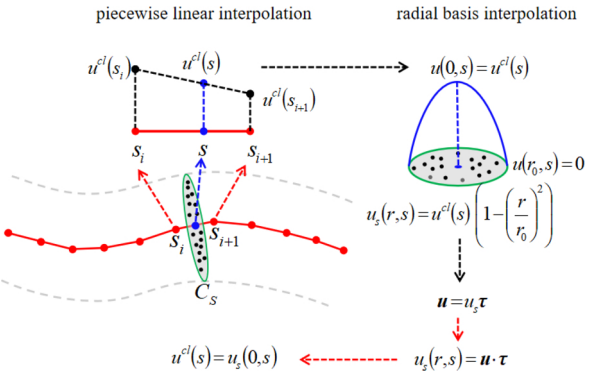

FIG. 3. *Diagram of the extension process from the 1D space to the 3D space by piecewise linear and radial basis interpolations. First obtain the value at the point on the centerline (blue point) of the cross section (green section) by linear interpolation and then use it to obtain the value at the mesh points (black points) on the cross section by a radial basis interpolation.*

3.1.2. 1D-3D restriction and extension matrices. Let $\{\boldsymbol{x}_i\}_{i=1}^{N}$ and $\{\boldsymbol{x}(s_i)\}_{i=1}^{N_{cl}}$ be the collection of mesh points of $\mathcal{T}_h$ and $\mathcal{T}_h^{cl}$, respectively. Denote $\{I_i\}_{i=1}^{N_{cl}-1}$ as the collection of line elements of $\mathcal{T}_h^{cl}$. Then for any s in $\mathcal{T}_h^{cl}$, there exists a unique $j \in \{1,\dots,N_{cl}-1\}$, denoted by $j(s)$, such that $s \in I_j$. Define a mapping $\mathcal{I}:\{\boldsymbol{x}_i\}_{i=1}^{N} \to \{I_i\}_{i=1}^{N_{cl}-1}$ by

$$\mathcal{I}(\boldsymbol{x}_i) = I_j,$$

where $j = \min_{s\in s^*} j(s)$ and $s^* = \arg\min_{s\in\mathcal{T}_h^{cl}} |\boldsymbol{x}_i - \boldsymbol{x}(s)|$. We define an extension operator from $(u_h^{cl}, p_h^{cl}) \in V_h^{cl} \times Q_h^{cl}$ to $(\boldsymbol{u}_h, p_h) \in V_h \times Q_h$ as

$$\boldsymbol{u}_h(\boldsymbol{x}_j) = u_h^{cl}(s)\zeta\left(\frac{|\boldsymbol{x}_j - \boldsymbol{x}(s)|}{r_0(s)}\right)\boldsymbol{\tau}(s), \quad p_h(\boldsymbol{x}_j) = p_h^{cl}(s) \tag{3.15}$$

for any $\boldsymbol{x}_j$ $(j=1,\dots,N)$ with s satisfying $s \in \mathcal{I}(\boldsymbol{x}_j)$ and $\boldsymbol{x}_j \in C_s(s)$. The extension operator (3.15) can be described in two steps for a nonbifurcating artery as shown in Figure 3: (1) first for each line segment $[s_i, s_{i+1}]$ we compute the value of the function at $s \in [s_i, s_{i+1}]$ by the piecewise linear interpolation; (2) we compute the values of the function for mesh points on the cross section $C_s(s)$ by the parabolic radial basis interpolation. For any $\boldsymbol{x}_j$, we denote $r_j = |\boldsymbol{x}_j - \boldsymbol{x}(s)|$, where s satisfies $s \in \mathcal{I}(\boldsymbol{x}_j)$ and $\boldsymbol{x}_j \in C_s(s)$. Let the influence set D_i of s_i be defined as

$$D_i = \left\{\boldsymbol{x} \in \{\boldsymbol{x}_i\}_{i=1}^{N} : \mathcal{I}(\boldsymbol{x}) \subset [s_{i-1}, s_{i+1}],\, \boldsymbol{x} \in C_s(s),\, \forall s \in [s_{i-1}, s_{i+1}]\right\}.$$

Below we describe the detailed algorithm to compute the 3D-1D restriction and 1D-3D extension matrices.

3.2. Multiscale two-level additive Schwarz preconditioner. In this subsection, we introduce a multiscale restricted additive Schwarz preconditioner consisting of a 1D coarse preconditioner and some overlapping 3D subdomain preconditioners. Let us first divide the arterial domain Ω into np nonoverlapping subdomains $\{\Omega_i\}_{i=1}^{np}$ such that each subdomain Ω_i consists of some elements in $\mathcal{T}_h$ denoted by $\mathcal{T}_{h,i}$, i.e., $\mathcal{T}_h = \bigcup_{i=1}^{np} \mathcal{T}_{h,i}$, where $\mathcal{T}_{h,i} \cap \mathcal{T}_{h,j} = \emptyset$ for $i \neq j$. In practice, this step is often realized by some graph partitioning libraries such as METIS or ParMETIS [31]. Then

Algorithm 3.2 Computation of the 3D-1D restriction matrix R_{cl} and 1D-3D extension matrix E_{cl}

1: Construct the $N_{cl} \times N$ weighting matrices $W^u = (w^u_{i,j})$ for the velocity and $W^p = (w^p_{i,j})$ for the pressure with the weighting coefficients

$$w^u_{i,j} = \begin{cases} \zeta\left(\frac{r_j}{r_0}\right)\phi_i(s), & \boldsymbol{x}_j \in D_i, \boldsymbol{x}_j \in C_s(s), \\ 0, & \boldsymbol{x}_j \notin D_i, \end{cases} \quad w^p_{i,j} = \begin{cases} \psi_i(s), & \boldsymbol{x}_j \in D_i, \boldsymbol{x}_j \in C_s(s), \\ 0, & \boldsymbol{x}_j \notin D_i, \end{cases}$$

where $\{\phi_i\}_{i=1}^{N_{cl}}$ are the nodal basis functions of S_h^{cl} and $\psi_i(s)$ is a function of s.

2: Calculate the $N_{cl} \times N_{cl}$ tangent matrices T_k $(k = 1, 2, 3)$ as

$$T_k := \operatorname{diag}\left(\tau^k(s_1), \ldots, \tau^k(s_{N_{cl}})\right), \tag{3.16}$$

where $\tau^k(s_i)$ is the kth component of the unit tangent vector $\boldsymbol{\tau}$ at the mesh point s_i.

3: Construct the $2N_{cl} \times 4N$ restriction matrix R_{cl} by

$$R_{cl} = \begin{pmatrix} W_1^u & W_2^u & W_3^u & 0 \\ 0 & 0 & 0 & W^p \end{pmatrix}, W_k^u = T_k W^u \, (k = 1, 2, 3) \tag{3.17}$$

with $\psi_i(s) = 1$ in W^p.

4: Construct the $4N \times 2N_{cl}$ extension matrix E_{cl} by

$$E_{cl} = \begin{pmatrix} W_1^u & W_2^u & W_3^u & 0 \\ 0 & 0 & 0 & W^p \end{pmatrix}^T, W_k^u = T_k W^u \, (k = 1, 2, 3) \tag{3.18}$$

with $\psi_i(s) = \phi_i(s)$ in W^p.

we obtain the overlapping subdomains $\{\Omega_i^\delta\}_{i=1}^{np}$ with the mesh $\mathcal{T}_{h,i}^\delta$ by extending each subdomain Ω_i with δ layers of elements from neighboring subdomains (see Figure 4), i.e.,

$$\mathcal{T}_{h,i}^0 = \mathcal{T}_{h,i}, \quad \mathcal{T}_{h,i}^\delta = \left\{ K \in \mathcal{T}_h : \exists K' \in \mathcal{T}_{h,i}^{\delta-1}, \partial K' \cap \partial K \neq \emptyset \right\}.$$

For each overlapping subdomain Ω_i^δ, the corresponding local finite element space is defined by

$$\boldsymbol{V}_h^i = \left\{ \boldsymbol{v} \in V_h|_{\Omega_i^\delta} : \boldsymbol{v}|_{\partial\Omega_i^\delta \setminus (\partial\Omega \setminus \Gamma_W)} = 0 \right\}, \; P_h^i = \left\{ q \in P_h|_{\Omega_i^\delta} : q|_{\partial\Omega_i^\delta \setminus \partial\Omega} = 0 \right\}.$$

Let $R_i : \boldsymbol{V}_h \times P_h \to \boldsymbol{V}_h^i \times P_h^i$ be a restriction operator which returns all degrees of freedom associated with the subspace $V_h^i \times P_h^i$ and the transpose R_i^T of R_i be the extension operator. Similarly we denote R_i^0 as a restriction operator associated with the nonoverlapping subdomains. Let A be the Jacobian matrix J_k^n and $A_i = R_i A R_i^T$ be the ith subdomain matrix. Then the one-level restricted additive Schwarz preconditioner [6] can be defined as

$$M_{1s}^{-1} = \sum_{i=1}^{np} (R_i^0)^T A_i^{-1} R_i. \tag{3.19}$$

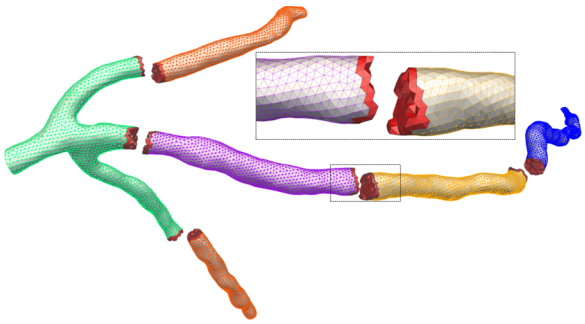

FIG. 4. *Example of nonoverlapping and overlapping partitions of an arterial domain with one overlapping layer, where the red elements represent the overlapping part.*

Finally, combining the coarse preconditioner (3.5) with the one-level preconditioner (3.19), we obtain the two-level additive Schwarz preconditioner

$$M_{2s,cl}^{-1} = M_{cl}^{-1} + M_{1s}^{-1} = E_{cl} A_{cl}^{-1} R_{cl} + \sum_{i=1}^{np} (R_i^0)^T A_i^{-1} R_i. \tag{3.20}$$

In (3.20), the matrix A_{cl} derived from the discretization of the 1D problem depends on the model parameter β. When $\beta = 0$, it means that the coarse problem is the 1D Stokes problem and A_{cl} in Algorithm 3.1 stays unchanged for each time and Newton step. When $\beta = 1$, the 1D problem represents a linearized unsteady incompressible Navier–Stokes problem and consequently A_{cl} needs to be recalculated at each time step based on the solution at the previous time step. In our implementation, for this case, u_h^{cl} at the previous time step is obtained by an interpolation of $\boldsymbol{u}_h$ because the original 1D problem (3.13) is not solved. Note that in (3.20) the coarse preconditioner and the one-level Schwarz preconditioner are added together; other hybrid versions [7, 61] can also be designed.

In this paper, we focus on the Newtonian model for the blood flows: the non-Newtonian effect is important for some situations [4, 22, 23, 29, 30, 39] and we expect that the extension of the proposed algorithm to non-Newtonian Navier–Stokes equations is straightforward [57].

4. Numerical experiments. In this section, we provide some numerical experiments to illustrate the effectiveness of the multiscale two-level restricted additive Schwarz preconditioner for unsteady incompressible Navier–Stokes flows in 3D patient-specific arteries. For the blood flows, we set the viscosity $\nu = 0.035$ g/(cm·s), the density $\rho = 1$ g/cm^3, and the source function $\boldsymbol{f} = 0$. On each outlet Γ_O^i, the resistance satisfies $R_i = R_{total}(\sum_{j=1}^m |\Gamma_O^j| / |\Gamma_O^i|)^{1.5}$ with a total resistance constant R_{total} to be given for each test case later [7]. The BDF2 with $\triangle t = 0.005$ s is used for the temporal discretization and the stabilized $\mathrm{P}_1 - \mathrm{P}_1$ finite element method is used for the spatial discretization. At each time step, we solve the nonlinear system by an inexact Newton method with a line search technique. At each Newton step, the Jacobian system is solved by the right-preconditioned GMRES(30) method. The default parameters of Newton and GMRES stopping conditions in Algorithm 3.1 are $rtol_{\text{Newton}} = 10^{-4}, atol_{\text{Newton}} = 10^{-6}$ and $rtol_{\text{GMRES}} = 10^{-4}, atol_{\text{GMRES}} = 10^{-6}$. For the Schwarz preconditioners, we choose the overlapping parameter $\delta = 1$ and ILU with one fill-in level is used to solve the subdomain problems. In the experiments, we consider a tube and two patient-specific arteries with different 3D fine meshes

TABLE 1

Details of 3D fine meshes used in the experiments. N, E, and h are the number of mesh points, the number of elements, and the approximate mesh size, respectively.

Tube			Three-branch artery			Twelve-branch artery		
N	E	h (mm)	N	E	h (mm)	N	E	h (mm)
1789	8179	1.690	30114	147223	0.289	87866	380332	0.276
12542	65432	0.846	144701	752741	0.174	243013	1130531	0.188
93659	523456	0.422	1079408	6024816	0.087	1497225	8050242	0.100

TABLE 2

Details of 1D coarse meshes used in the experiments. N_{cl} and h_{cl} are the number of mesh points and the approximate mesh size of the centerline, respectively.

Tube		Three-branch artery		Twelve-branch artery	
N_{cl}	h_{cl} (mm)	N_{cl}	h_{cl} (mm)	N_{cl}	h_{cl} (mm)
100	0.505	247	0.609	677	0.879

(Table 1) and 1D coarse meshes (Table 2). For the 1D coarse preconditioner, there are two models to use, i.e., the Stokes model ($\beta = 0$) and the Navier–Stokes model ($\beta = 1$). For the test problems considered in this paper, the Stokes model is quite efficient in terms of the number of GMRES iterations and the coarse preconditioner needs to be computed only once for all time steps and all Newton iterations (the subdomain matrices are recomputed at every Newton iteration), therefore in the following experiments, we use the Stokes model for most of the tests. In the end of the section we show some numerical results when the Navier–Stokes model is used. Note that in the following tables we only report the average number of GMRES iterations per Newton iteration and the average number of Newton iterations per time step is reported when the calculation is for a full cardiac cycle.

4.1. Womersley flow in a tube. We first verify the correctness of the implementation of the proposed algorithm by the Womersley flow in a tube with length $L_{tube} = 5$ cm and radius $R_{tube} = 0.5$ cm. It is known that (2.1) has the following analytic solution [20],

$$u(r,t) = -\frac{R_{tube}^2}{\nu w_o^2}\left(\sin(t)J_1(r) + \cos(t)J_2(r)\right), v = 0, w = 0, p(x,t) = \cos(t)\left(x - \frac{L_{tube}}{2}\right),$$

where $r = \sqrt{y^2 + z^2}$, $w_o = R_{tube}\sqrt{\rho/\nu}$ is the Womersley number, $J_1(r)$, $J_2(r)$ are the real and imaginary parts of $J(r) = 1 - J_0(\Lambda\frac{r}{R_{tube}})J_0(\Lambda)^{-1}, \Lambda = w_o e^{i\frac{3}{4}\pi}$ with the zeroth order Bessel function of the first kind J_0. For the boundary conditions, on the inlet the velocity is set to satisfy the exact velocity solution and on the outlet we set $R_{total} = 0$ dyn·s/cm^5 to be consistent with the exact pressure solution. We compute the solution for a period of $[0, 2\pi]$ with $\triangle t = \pi/100$ and test three unstructured meshes described in Table 1. For this case, the maximum Reynolds number in a period is about 15. Figure 5 shows the numerical results of the velocity profile, the distributions, and the errors of the magnitude of the velocity and the average pressure difference between the inlet and the outlet. We can see that the numerical solutions gradually converge to the analytic solution with the use of finer meshes and the numerical solution with $N = 93659$ is quite close to the analytical solution, which indicates the correctness of the implementation. Table 3 shows the average

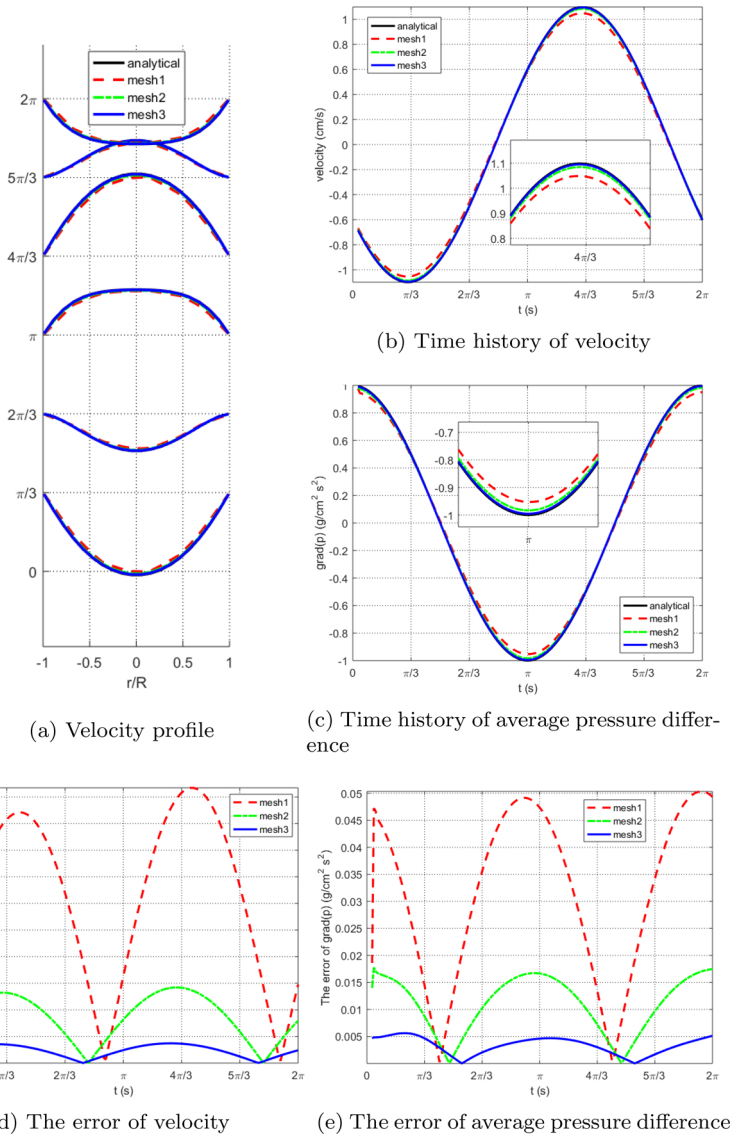

(a) Velocity profile

(b) Time history of velocity

(c) Time history of average pressure difference

(d) The error of velocity

(e) The error of average pressure difference

FIG. 5. *A comparison of the analytical solution and the numerical solution obtained with three meshes with* 1789, 12542, *and* 93659 *mesh points labeled by "mesh*1*", "mesh*2*," and "mesh*3*", respectively. (a): the velocity profile on the cross section* $x = 0$ *at different times* $t = \pi/3, 2\pi/3, \pi, 4\pi/3, 5\pi/3, 2\pi$. *(b): the time history of the velocity at the center* $(0, 0, 0)$ *of the tube. (c): the time history of the average pressure difference scaled by the length of the tube, i.e., the ratio of the pressure difference between the inlet and the outlet and the length of the tube. (d): the error of the velocity shown in subfigure (b). (e): the error of the average pressure difference shown in subfigure (c). Note that the black solid line is covered by other lines.*

number of Newton iterations at each time step and the average number of GMRES iterations at each Newton step with different preconditioners. The number of Newton iterations is almost independent of the fine mesh size, the coarse mesh size, the number of subdomains, and the preconditioners, but the number of GMRES iterations is sensitive to the fine mesh size and the preconditioner. Compared with the one-level

TABLE 3

A comparison of the one-level and two-level preconditioners in terms of the average number of Newton iterations per time step and the average number of GMRES iterations per Newton iteration in a full period for the Womersley flow. N is the total number of mesh points, and np is the number of subdomains.

		One-level		Two-level		
N	np	Newton	GMRES	N_{cl}	Newton	GMRES
1789	8	1.74	12.06	34	1.84	5.74
12542	16	1.87	17.84	100	1.86	5.74
93659	32	1.88	29.43	100	1.84	6.46

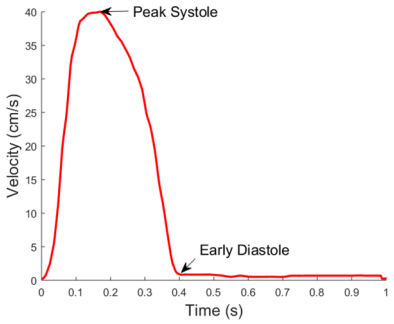

FIG. 6. *The velocity pulse at the center of the inlet for a cardiac cycle.*

preconditioner, the new two-level preconditioner offers a better GMRES convergence and scalability with respect to the fine mesh size for this case.

4.2. Patient-specific arteries. In this subsection, we focus on two patient-specific arteries, including a three-branch artery and a twelve-branch artery. For the three-branch artery, there is one inlet with diameter 2.30 mm and three outlets with diameters 1.36 mm, 1.30 mm, and 1.00 mm. For the twelve-branch artery, there is one inlet with diameter 3.00 mm and twelve outlets with diameters about 1.00 mm. On the inlet, we prescribe a pulsatile periodic flow velocity (see Figure 6) with the parabolic profile. On the outlet, we set $R_{total} = 1500$ dyn·s/cm^5. Three different unstructured meshes (see Table 1) for both arteries are considered. Note that the maximum Reynolds number is about 260 for the three-branch case and 340 for the twelve-branch case. For the two-level method, the coarse mesh information is given in Table 2.

First for the three-branch artery, we show the time histories of the velocity and pressure at different points for a cardiac cycle in Figure 7. These curves of the velocity and pressure have similar waveforms to the inlet flow waveform. Figure 8 displays local features near the bifurcation at different phases. The velocity profiles have noticeable differences at the peak systole and early diastole phases. The maximum value of the velocity magnitude happens in areas close to the wall and the corner of the bifurcation at the peak systole phase, but move to the internal center at the early diastole phase. The pressure at the corner of the bifurcation reaches the local maximum for both phases and the obvious vortex occurs at the early diastole. In Tables 4 and 5, we give the number of Newton iterations and the average number of GMRES iterations at each Newton step of the one-level and two-level methods at the peak systole and the early diastole, respectively. Compared to the early diastole case,

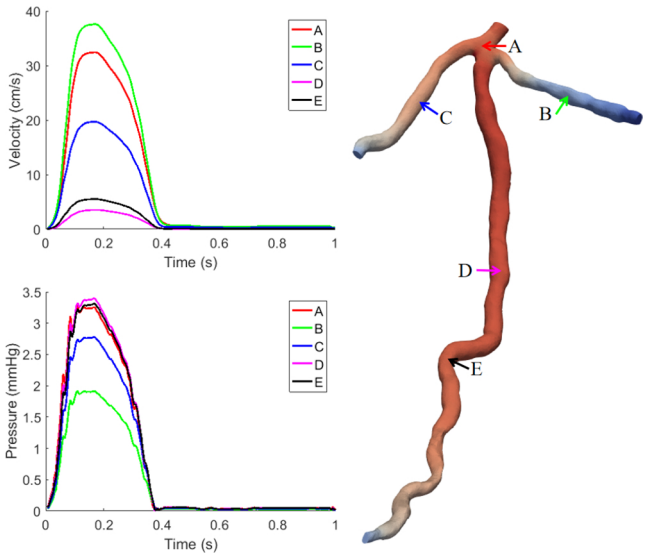

FIG. 7. *The time histories of the velocity and pressure at different points for a cardiac cycle.*

both methods require more GMRES iterations at the peak systole. For both phases, the two-level method scales much better with respect to the fine mesh size and the number of subdomains, but the one-level method performs poorly, especially on the fine mesh.

Further we consider the more complicated twelve-branch artery. Figure 9 shows the magnitude of the velocity and the wall shear stress at different locations at the peak systole and the wall shear stress is defined by

$$wss := -\nu \nabla \boldsymbol{u} \cdot \boldsymbol{n} + ((\nu \nabla \boldsymbol{u} \cdot \boldsymbol{n}) \cdot \boldsymbol{n})\, \boldsymbol{n}.$$

Figure 10 shows the streamlines at the peak systole. In order to study the effectiveness of the two-level method for this case, we provide the number of iterations at the peak systole (Table 6) and the early diastole (Table 7) and observe similar behaviors as in the three-branch case. Comparing the three-branch case with the twelve-branch case, for the one-level method, we see that the number of GMRES iterations increases a lot, but the increase of the two-level method is not much. These results indicate that the proposed two-level method is effective and robust with respect to the complexity of the arterial geometry.

The above discussions focus on the performance of the proposed method at two different times in a cardiac cycle, namely, the peak systole phase when the velocity and pressure are near their maximum values and the early diastole phase when their respective values are close to their minimum. In Table 8 we illustrate the performance in a complete cardiac cycle. The average number of Newton iterations stays unchanged and the average number of GMRES iterations has a small increase when refining the mesh, and we can see that the two-level method works well for the full cardiac cycle. Next, we consider the impact of other algorithmic parameters including the ILU fill-in level, the overlapping parameter, and the coarse mesh size. Table 9 shows the number of iterations for different ILU fill-in levels and indicates that the ILU fill-in level has an obvious impact on the number of GMRES

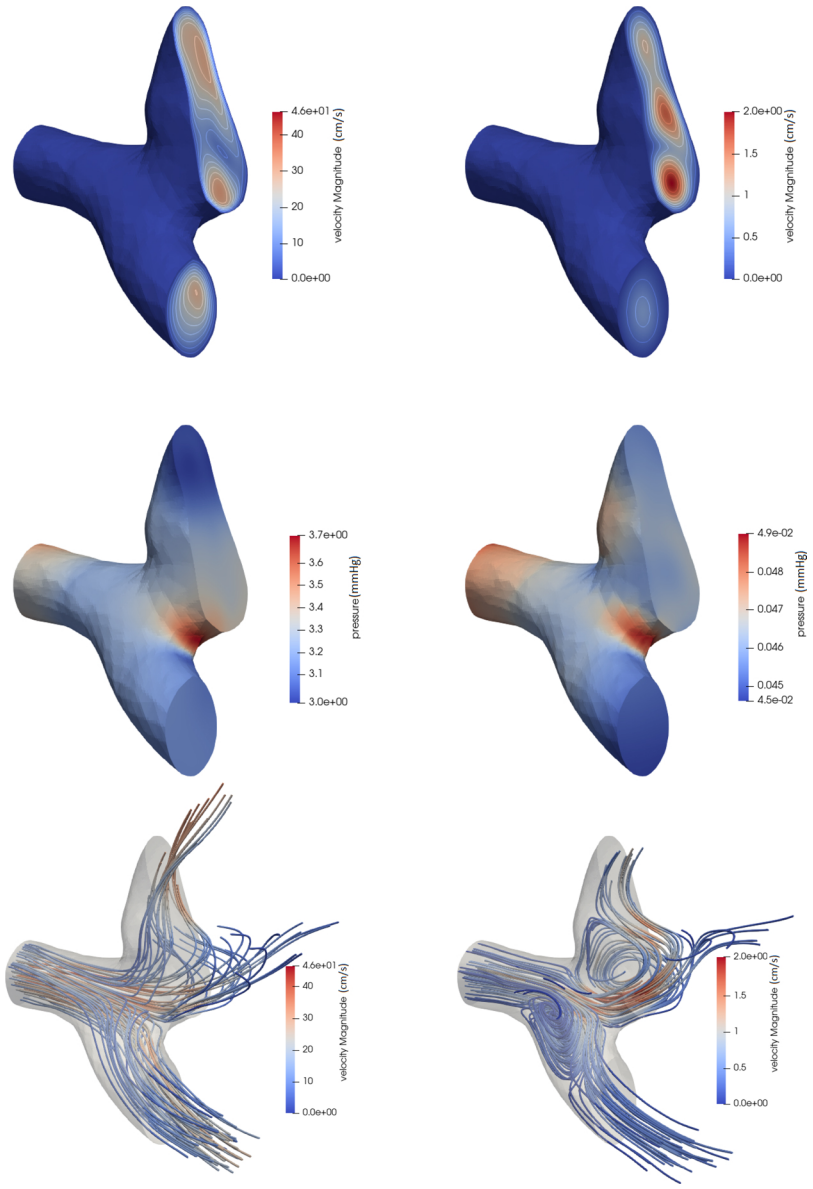

FIG. 8. *The distributions of the magnitude of the velocity (top), pressure (middle), and the streamline (bottom) near the bifurcation at the systole phase when* $t = 0.165$ *s (left) and the diastole phase when* $t = 0.405$ *s (right).*

iterations and ILU(2) can clearly improve the GMRES convergence. Considering the overlapping parameter, Table 10 shows that a small overlapping parameter is enough, which is consistent with the classical theory of two-level Schwarz methods in [13]. Table 11 lists the number of iterations with different coarse meshes and shows, as expected, that a finer coarse mesh provides a better GMRES convergence especially at the systole phase of a cardiac cycle.

TABLE 4

At the systole phase, a comparison of one-level and two-level preconditioners in terms of the number of iterations for the three-branch artery. N is the total number of mesh points and np is the number of subdomains.

			One-level		Two-level	
Phase	N	np	Newton	GMRES	Newton	GMRES
		16	2	297.50	2	19.50
	30114	32	2	307.50	2	19.50
		64	2	319.50	2	20.00
		32	2	583.50	2	24.50
Systole	144701	64	2	558.00	2	25.00
		128	2	633.50	2	24.00
		256	2	485.00	2	36.00
	1079408	512	2	807.50	2	36.00
		1024	2	1128.50	2	36.50

TABLE 5

At the diastole phase, a comparison of one-level and two-level preconditioners in terms of the number of iterations for the three-branch artery. N is the total number of mesh points and np is the number of subdomains.

			One-level		Two-level	
Phase	N	np	Newton	GMRES	Newton	GMRES
		16	2	156.50	2	15.00
	30114	32	2	134.00	2	15.00
		64	2	247.00	2	15.00
		32	2	226.50	2	17.00
Diastole	144701	64	2	222.50	2	17.50
		128	2	235.50	2	17.00
		256	2	244.50	2	25.00
	1079408	512	2	366.50	2	25.50
		1024	2	426.50	2	25.50

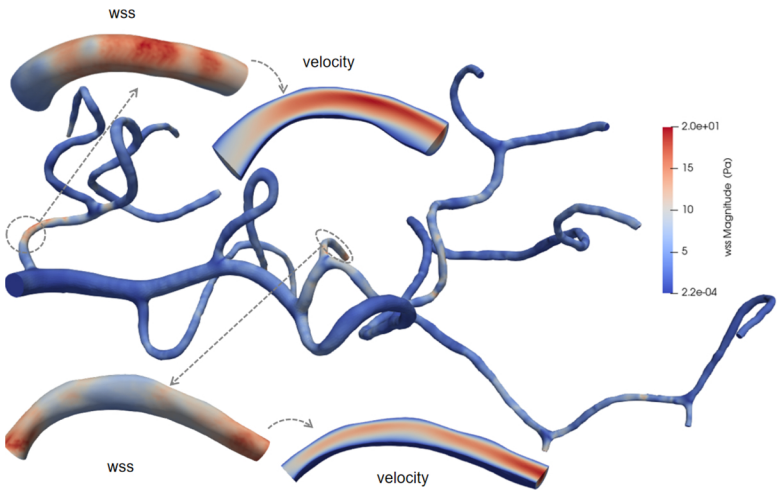

FIG. 9. *The wall shear stress and velocity magnitude at different locations at the peak systole.*

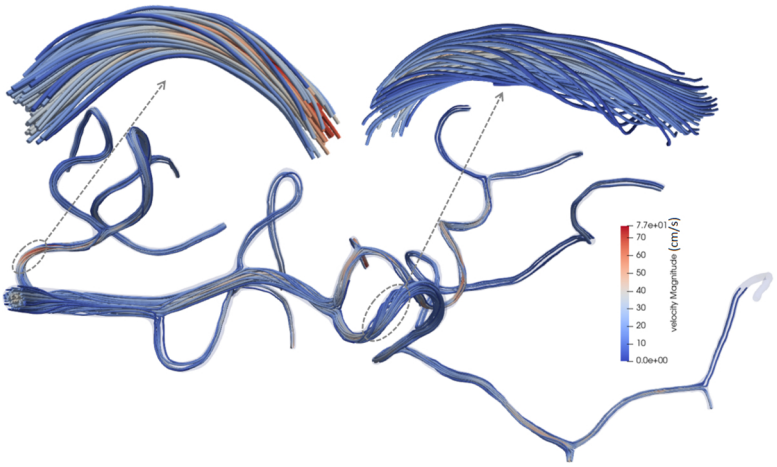

FIG. 10. *The streamlines at different locations at the peak systole.*

TABLE 6

At the systole phase, a comparison of one-level and two-level preconditioners in terms of the number of iterations for the twelve-branch artery. N is the total number of mesh points and np is the number of subdomains.

			One-level		Two-level	
Phase	N	np	Newton	GMRES	Newton	GMRES
		32	2	675.00	2	36.00
	87866	64	2	748.50	2	36.50
		128	2	845.50	2	36.00
		64	2	1318.50	2	41.00
Systole	243013	128	2	980.50	2	41.00
		256	2	1214.50	2	42.00
		256	4	2670.00	2	113.00
	1497225	512	3	2461.00	2	113.00
		1024	3	2841.33	2	112.00

Next, in Table 12, we present the performance of the 1D coarse preconditioner for different time step sizes when there is a stenosis in the artery. In this experiment, we test the three-branch artery with and without a stenosis which reduces the diameter of the artery by 50%, as shown in Figure 11. Figure 11 also shows the distribution of the pressure which decreases rapidly passing the stenosis. Table 12 indicates that with the increase of the time step size, the numbers of Newton and GMRES iterations both increase slightly.

Note that the coarse preconditioner in all the experiments presented so far in this section is constructed based on the 1D Stokes model ($\beta = 0$). In order to show the effect of the 1D Navier–Stokes model ($\beta = 1$) on the number of iterations, in Table 13, we provide a comparison of the number of iterations with different coarse models for the twelve-branch artery. We see that the 1D Navier–Stokes model moderately improves the GMRES convergence at the peak systole and the difference is quite small at the early diastole. Therefore we conclude that for problems considered in this paper, the Stokes model is sufficient, but for more complicated problems the Navier–Stokes model might be more useful.

TABLE 7

At the diastole phas,: a comparison of one-level and two-level preconditioners in terms of the number of iterations for the twelve-branch artery. N is the total number of mesh points and np is the number of subdomains.

			One-level		Two-level	
Phase	N	np	Newton	GMRES	Newton	GMRES
		32	2	279.00	2	26.00
	87866	64	2	280.00	2	25.50
		128	2	328.00	2	26.50
		64	2	412.00	2	26.50
Diastole	243013	128	2	425.00	2	26.50
		256	2	463.00	2	27.00
		256	2	651.50	2	62.50
	1497225	512	2	655.00	2	63.00
		1024	2	890.50	2	63.00

TABLE 8

The average number of iterations of the two-level preconditioner in a cardiac cycle for three-branch and twelve-branch arteries. N is the total number of mesh points and np is the number of subdomains.

Artery	N	np	Newton	GMRES
	30114	16	1.59	16.70
Three-branch	144701	32	1.58	18.56
	1079408	256	1.53	28.43
	87866	32	1.70	33.33
Twelve-branch	243013	64	1.69	33.68
	1497225	256	1.66	71.27

TABLE 9

The effect of the ILU fill-in level "LU" on the number of iterations of the two-level preconditioner.

		Three-branch		Twelve-branch	
Phase	ILU	Newton	GMRES	Newton	GMRES
	0	2	62.00	2	234.00
Systole	1	2	36.00	2	113.00
	2	2	29.50	2	72.00
	0	2	36.50	2	95.50
Diastole	1	2	25.00	2	62.50
	2	2	20.00	2	43.00

TABLE 10

The effect of the overlapping parameter δ on the number of iterations of two-level preconditioners.

		Three-branch		Twelve-branch	
Phase	δ	Newton	GMRES	Newton	GMRES
	1	2	36.00	2	113.00
Systole	2	2	35.00	2	104.00
	3	2	34.00	2	100.50
	1	2	25.00	2	62.50
Diastole	2	2	24.00	2	63.00
	3	2	22.50	2	63.00

TABLE 11

The effect of the number of coarse mesh points N_{cl} on the number of iterations of two-level preconditioners.

	Three-branch			Twelve-branch		
Phase	N_{cl}	Newton	GMRES	N_{cl}	Newton	GMRES
Systole	88	2	53.50	522	2	128.00
	128	2	46.50	677	2	113.00
	247	2	36.00	998	2	99.00
Diastole	88	2	38.00	522	2	64.00
	128	2	32.50	677	2	62.50
	247	2	25.00	998	2	61.00

TABLE 12

The performance of the 1D coarse preconditioner with respect to the time step size and the three-branch artery with and without a stenosis at $t = 0.16$ s. N is the total number of mesh points.

Geometry	N	$\triangle t$ (s)	Newton	GMRES
Norm	331370	0.005	2	30.00
		0.01	2	41.50
		0.02	3	46.00
Stenosis	329938	0.005	2	30.50
		0.01	2	44.50
		0.02	3	48.00

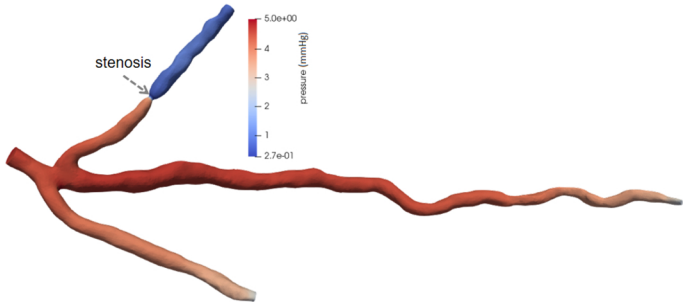

FIG. 11. *The distribution of the pressure at $t = 0.16$ s for the three-branch artery with a stenosis.*

5. Conclusions. Modeling blood flows using the 3D unsteady incompressible Navier–Stokes equations in patient-specific arteries with many bifurcating branches is computationally very expensive. In this paper, we developed a Newton–Krylov method with an effective two-level restricted additive Schwarz preconditioner consisting of overlapping 3D subdomain preconditioners and a 1D coarse preconditioner constructed by a parameterized unsteady Navier–Stokes model defined on the centerline of the artery with an appropriate 3D-1D restriction and 1D-3D extension operators. The key feature of the method is that the cost of the 1D coarse problem is almost negligible but it reduces significantly the number of GMRES iterations compared with the one-level method. Numerical experiments show that the proposed method is not only scalable in terms of the numbers of linear and nonlinear iterations, but is also quite robust with respect to the complex geometry of the artery and varying flow conditions. In future work, we plan to further develop the method for diseased arteries with, for example, an aneurysm or stenosis, as well as study its performance on large-scale parallel computers.

TABLE 13
A comparison of the coarse preconditioner with 1D Stokes ($\beta = 0$) and Navier–Stokes ($\beta = 1$) models in terms of the number of iterations. $rtol_{GMRES}$ is the GMRES relative tolerance.

		$\beta = 0$		$\beta = 1$	
Phase	$rtol_{\text{GMRES}}$	Newton	GMRES	Newton	GMRES
Systole	10^{-4}	2	113.00	2	89.50
	10^{-3}	2	94.00	2	77.50
	10^{-2}	2	85.00	2	78.00
Diastole	10^{-4}	2	62.50	2	63.00
	10^{-3}	2	45.00	2	45.00
	10^{-2}	2	36.00	2	36.00

REFERENCES

[1] M. S. Alnæs, J. Isaksen, K.-A. Mardal, B. Romner, M. K. Morgan, and T. Ingebrigtsen, *Computation of hemodynamics in the circle of Willis*, Stroke, 38 (2007), pp. 2500–2505.

[2] D. Balzani, D. Böse, D. Brands, R. Erbel, A. Klawonn, O. Rheinbach, and J. Schröder, *Parallel simulation of patient-specific atherosclerotic arteries for the enhancement of intravascular ultrasound diagnostics*, Engrg. Comput., 29 (2012).

[3] A. T. Barker and X.-C. Cai, *Scalable parallel methods for monolithic coupling in fluid-structure interaction with application to blood flow modeling*, J. Comput. Phys., 229 (2010), pp. 642–659.

[4] J. Bernsdorf and D. Wang, *Non-Newtonian blood flow simulation in cerebral aneurysms*, Comput. Math. Appl., 58 (2009), pp. 1024–1029.

[5] X.-C. Cai, W. D. Gropp, D. E. Keyes, R. G. Melvin, and D. P. Young, *Parallel Newton–Krylov–Schwarz algorithms for the transonic full potential equation*, SIAM J. Sci. Comput., 19 (1998), pp. 246–265.

[6] X.-C. Cai and M. Sarkis, *A restricted additive Schwarz preconditioner for general sparse linear systems*, SIAM J. Sci. Comput., 21 (1999), pp. 792–797.

[7] R. Chen, B. Wu, Z. Cheng, W.-S. Shiu, J. Liu, L. Liu, Y. Wang, X. Wang, and X.-C. Cai, *A parallel non-nested two-level domain decomposition method for simulating blood flows in cerebral artery of stroke patient*, Internat. J. Numer. Methods Biomed. Eng., 36 (2020), e3392.

[8] J. S. Coogan, J. D. Humphrey, and C. A. Figueroa, *Computational simulations of hemodynamic changes within thoracic, coronary, and cerebral arteries following early wall remodeling in response to distal aortic coarctation*, Biomech. Model. Mechanobiol., 12 (2013), pp. 79–93.

[9] J. E. Dennis Jr. and R. B. Schnabel, *Numerical Methods for Unconstrained Optimization and Nonlinear Equations*, Classics Appl Math. 16, SIAM, Philadelphia, PA, 1996.

[10] S. Deparis, D. Forti, G. Grandperrin, and A. Quarteroni, *FaCSI: A block parallel preconditioner for fluid-structure interaction in hemodynamics*, J. Comput. Phys., 327 (2016), pp. 700–718.

[11] S. Deparis, G. Grandperrin, and A. Quarteroni, *Parallel preconditioners for the unsteady Navier-Stokes equations and applications to hemodynamics simulations*, Comput. Fluids, 92 (2014), pp. 253–273.

[12] C. R. Dohrmann, A. Klawonn, and O. B. Widlund, *Domain decomposition for less regular subdomains: Overlapping Schwarz in two dimensions*, SIAM J. Numer. Anal., 46 (2008), pp. 2153–2168.

[13] M. Dryja and O. B. Widlund, *Domain decomposition algorithms with small overlap*, SIAM J. Sci. Comput., 15 (1994), pp. 604–620.

[14] H. Elman, V. E. Howle, J. Shadid, R. Shuttleworth, and R. Tuminaro, *A taxonomy and comparison of parallel block multi-level preconditioners for the incompressible Navier-Stokes equations*, J. Comput. Phys., 227 (2008), pp. 1790–1808.

[15] C. Fisher and J. S. Rossmann, *Effect of non-Newtonian behavior on hemodynamics of cerebral aneurysms*, J. Biomech. Eng., 131 (2009), 091004.

[16] L. Formaggia, J.-F. Gerbeau, F. Nobile, and A. Quarteroni, *On the coupling of 3D and 1D Navier-Stokes equations for flow problems in compliant vessels*, Comput. Methods Appl. Mech. Engrg., 191 (2001), pp. 561–582.

[17] L. Formaggia, D. Lamponi, and A. Quarteroni, *One-dimensional models for blood flow in arteries*, J. Engrg. Math., 47 (2003), pp. 251–276.

[18] L. Formaggia, F. Nobile, A. Quarteroni, and A. Veneziani, *Multiscale modelling of the circulatory system: A preliminary analysis*, Comput. Vis. Sci., 2 (1999), pp. 75–83.
[19] L. P. Franca and S. L. Frey, *Stabilized finite element methods.* II. *The incompressible Navier-Stokes equations*, Comput. Methods Appl. Mech. Engrg., 99 (1992), pp. 209–233.
[20] Y. C. Fung, *Biomechanics: Motion, Flow, Stress, and Growth*, Springer, New York, 1990.
[21] M. W. Gee, U. Küttler, and W. A. Wall, *Truly monolithic algebraic multigrid for fluid-structure interaction*, Internat. J. Numer. Methods Engrg., 85 (2011), pp. 987–1016.
[22] F. Gijsen, E. Allanic, F. Van De Vosse, and J. Janssen, *The influence of the non-Newtonian properties of blood on the flow in large arteries: Unsteady flow in a 90 degrees curved tube*, J. Biomech. 32 (1999), pp. 705–713.
[23] F. J. Gijsen, F. N. van de Vosse, and J. Janssen, *The influence of the non-Newtonian properties of blood on the flow in large arteries: Steady flow in a carotid bifurcation model*, J. Biomech., 32 (1999), pp. 601–608.
[24] L. Grinberg, E. Cheever, T. Anor, J. R. Madsen, and G. Karniadakis, *Modeling blood flow circulation in intracranial arterial networks: A comparative 3D/1D simulation study*, Ann. Biomed. Eng., 39 (2011), pp. 297–309.
[25] L. Grinberg, D. A. Fedosov, and G. E. Karniadakis, *Parallel multiscale simulations of a brain aneurysm*, J. Comput. Phys., 244 (2013), pp. 131–147.
[26] J. L. Guermond, P. Minev, and J. Shen, *An overview of projection methods for incompressible flows*, Comput. Methods Appl. Mech. Engrg., 195 (2006), pp. 6011–6045.
[27] A. Heinlein, C. Hochmuth, and A. Klawonn, *Monolithic overlapping Schwarz domain decomposition methods with GDSW coarse spaces for incompressible fluid flow problems*, SIAM J. Sci. Comput., 41 (2019), pp. C291–C316.
[28] A. Heinlein, C. Hochmuth, and A. Klawonn, *Reduced dimension GDSW coarse spaces for monolithic Schwarz domain decomposition methods for incompressible fluid flow problems*, Internat. J. Numer. Methods Engrg., 121 (2020), pp. 1101–1119.
[29] B. M. Johnston, P. R. Johnston, S. Corney, and D. Kilpatrick, *Non-Newtonian blood flow in human right coronary arteries: Steady state simulations*, J. Biomech., 37 (2004), pp. 709–720.
[30] B. M. Johnston, P. R. Johnston, S. Corney, and D. Kilpatrick, *Non-Newtonian blood flow in human right coronary arteries: Transient simulations*, J. Biomech., 39 (2006), pp. 1116–1128.
[31] G. Karypis and V. Kumar, *Multilevel k-way partitioning scheme for irregular graphs*, J. Parallel Distrib. Comput., 48 (1998), pp. 96–129.
[32] A. Klawonn, *An optimal preconditioner for a class of saddle point problems with a penalty term*, SIAM J. Sci. Comput., 19 (1998), pp. 540–552.
[33] A. Klawonn, *Block-triangular preconditioners for saddle point problems with a penalty term*, SIAM J. Sci. Comput., 19 (1998), pp. 172–184.
[34] A. Klawonn and L. F. Pavarino, *Overlapping Schwarz methods for mixed linear elasticity and Stokes problems*, Comput. Methods Appl. Mech. Engrg., 165 (1998), pp. 233–245.
[35] D. A. Knoll and D. E. Keyes, *Jacobian-free Newton-Krylov methods: A survey of approaches and applications*, J. Comput. Phys., 193 (2004), pp. 357–397.
[36] D. A. Knoll and W. J. Rider, *A multigrid preconditioned Newton–Krylov method*, SIAM J. Sci. Comput., 21 (1999), pp. 691–710.
[37] F. Kong and X.-C. Cai, *A highly scalable multilevel Schwarz method with boundary geometry preserving coarse spaces for 3D elasticity problems on domains with complex geometry*, SIAM J. Sci. Comput., 38 (2016), pp. C73–C95.
[38] F. Kong and X.-C. Cai, *A scalable nonlinear fluid-structure interaction solver based on a Schwarz preconditioner with isogeometric unstructured coarse spaces in* $3D$, J. Comput. Phys., 340 (2017), pp. 498–518.
[39] J. Lee and N. Smith, *Development and application of a one-dimensional blood flow model for microvascular networks*, Proc. Inst. Mech. Eng. H J. Eng. Med., 222 (2008), pp. 487–511.
[40] J. Li and O. Widlund, *BDDC algorithms for incompressible Stokes equations*, SIAM J. Numer. Anal., 44 (2006), pp. 2432–2455.
[41] Z. Lin, R. Chen, B. Gao, S. Qin, B. Wu, J. Liu, and X.-C. Cai, *A highly parallel simulation of patient-specific hepatic flows*, Internat. J. Numer. Methods Biomed. Eng., 37 (2021), e3451.
[42] Y. Liu and X.-C. Cai, *A central-line coarse preconditioner for Stokes flows in artery-like domains*, Numer. Algorithms, 87 (2021), pp. 137–160.
[43] J. M. Murabito, R. B. D'Agostino, H. Silbershatz, and P. W. Wilson, *Intermittent claudication: A risk profile from the Framingham heart study*, Circulation, 96 (1997), pp. 44–49.

[44] S. Qin, B. Wu, J. Liu, W.-S. Shiu, Z. Yan, R. Chen, and X.-C. Cai, *Efficient parallel simulation of hemodynamics in patient-specific abdominal aorta with aneurysm*, Comput. Biol. Med., 136 (2021), 104652.

[45] S. Qin, B. Wu, J. Liu, W.-S. Shiu, Z. Yan, R. Chen, and X.-C. Cai, *Numerical simulation of blood flows in patient-specific abdominal aorta with primary organs*, Biomech. Model. Mechanobiol., 20 (2021), pp. 909–924.

[46] A. Quarteroni and L. Formaggia, *Mathematical modelling and numerical simulation of the cardiovascular system*, in Computational Models for the Human Body, Handb. Numer. Anal. 12, North-Holland, Amsterdam, 2004, pp. 3–127.

[47] A. Quarteroni, A. Manzoni, and C. Vergara, *The cardiovascular system: Mathematical modelling, numerical algorithms and clinical applications*, Acta Numer., 26 (2017), pp. 365–590.

[48] A. Quarteroni, F. Saleri, and A. Veneziani, *Analysis of the Yosida method for the incompressible Navier-Stokes equations*, J. Math. Pures Appl. (9), 78 (1999), pp. 473–503.

[49] A. Quarteroni, F. Saleri, and A. Veneziani, *Factorization methods for the numerical approximation of Navier-Stokes equations*, Comput. Methods Appl. Mech. Engrg., 188 (2000), pp. 505–526.

[50] A. Quarteroni, M. Tuveri, and A. Veneziani, *Computational vascular fluid dynamics: Problems, models and methods*, Comput. Vis. Sci., 2 (2000), pp. 163–197.

[51] A. Randles, E. W. Draeger, T. Oppelstrup, L. Krauss, and J. A. Gunnels, *Massively parallel models of the human circulatory system*, in Proceedings of the International Conference for High Performance Computing, Networking, Storage and Analysis, SC '15, New York, Association for Computing Machinery, New York, 2015, pp. 1–11.

[52] P. Reymond, F. Merenda, F. Perren, D. Rufenacht, and N. Stergiopulos, *Validation of a one-dimensional model of the systemic arterial tree*, Amer. J. Physiol. Heart Circ. Physiol., 297 (2009), pp. H208–H222.

[53] P. Reymond, F. Perren, F. Lazeyras, and N. Stergiopulos, *Patient-specific mean pressure drop in the systemic arterial tree, a comparison between* 1*-D and* 3*-D models*, J. Biomech., 45 (2012), pp. 2499–2505.

[54] Y. Saad, *Iterative Methods for Sparse Linear Systems*, 2nd ed., SIAM, Philadelphia, 2003.

[55] D. M. Sforza, C. M. Putman, and J. R. Cebral, *Hemodynamics of cerebral aneurysms*, Annu. Rev. Fluid Mech., 41 (2009), pp. 91–107.

[56] S. Sherwin, V. Franke, J. Peiro, and K. Parker, *One-dimensional modelling of a vascular network in space-time variables*, J. Engrg. Math., 47 (2003), pp. 217–250.

[57] W.-S. Shiu, F.-N. Hwang, and X.-C. Cai, *Parallel domain decomposition method for finite element approximation of* 3 *steady state non-Newtonian fluids*, Internat. J. Numer. Methods Fluids, 78 (2015), pp. 502–520.

[58] N. P. Smith, A. J. Pullan, and P. J. Hunter, *An anatomically based model of transient coronary blood flow in the heart*, SIAM J. Appl. Math., 62 (2002), pp. 990–1018.

[59] C. A. Taylor, T. J. Hughes, and C. K. Zarins, *Finite element modeling of blood flow in arteries*, Comput. Methods Appl. Mech. Engrg., 158 (1998), pp. 155–196.

[60] C. A. Taylor and J. D. Humphrey, *Open problems in computational vascular biomechanics: Hemodynamics and arterial wall mechanics*, Comput. Methods Appl. Mech. Engrg., 198 (2009), pp. 3514–3523.

[61] A. Toselli and O. Widlund, *Domain Decomposition Methods-Algorithms and Theory*, Springer, Berlin, 2005.

[62] I. E. Vignon-Clementel, C. A. Figueroa, K. E. Jansen, and C. A. Taylor, *Outflow boundary conditions for three-dimensional finite element modeling of blood flow and pressure in arteries*, Comput. Methods Appl. Mech. Engrg., 195 (2006), pp. 3776–3796.

[63] Y. Zhang, Y. Bazilevs, S. Goswami, C. L. Bajaj, and T. J. Hughes, *Patient-specific vascular NURBS modeling for isogeometric analysis of blood flow*, Comput. Methods Appl. Mech. Engrg., 196 (2007), pp. 2943–2959.